International Journal of Earth Sciences (2026) 115:46
https://doi.org/10.1007/s00531-026-02593-8

ORIGINAL PAPER

Host-rock compositions and fluid inclusion characteristics associated with epithermal Au–Ag mineralization at Galim-Legalgorou, Cameroon

Terence Cho Ngang[1,2] · Thomas Wagner[2] · Jessica A. Stammeier[3] · Cheo Emmanuel Suh[1,4] · Tasin Godlove Bafon[1,5] · Tobias Fusswinkel[2] · Ralain Bryan Ngatcha[1,5] · Akumbom Vishiti[6] · Eric-Claude Essono Owona[7]

Received: 3 November 2025 / Accepted: 23 May 2026

Abstract

The Galim-Legalgorou Au–Ag prospect in Northwestern Cameroon has been recently classified as epithermal based on the wall-rock alteration assemblages, ore mineralogy, and chemistry of electrum plus sphalerite. However, questions regarding the host-rock compositions and how these may have interacted with mineralizing fluids remained unanswered. This study presents the host-rock compositions as well as features of quartz-hosted fluid inclusions related to mineralization. Whole-rock major element data show a highly evolved magmatic rock series from basalt to rhyolite, with the latter being the major host to the mineralization. Rare-earth element data of the trachyte and rhyolites show a slight enrichment trend in LREE relative to HREE, with a negative europium anomaly ($\{Eu/Eu^*\}_{CN} = 0.09$ to 0.51), suggestive of plagioclase fractionation at the magma source. Coexisting liquid-rich and vapor-rich secondary fluid inclusions are consistent with boiling and vapor loss during the late stages of fluid evolution. LA-ICP-MS data show that Na and K are the dominant ions in fluid inclusions, suggesting that the fluid was in equilibrium with alkali-rich host rocks at the time of mineralization. Homogenization temperatures of 180–303 °C (average ~ 273 °C), with salinities around 2.2 wt% $NaCl_{eq}$., and Na–K geothermometry indicate trapping conditions near the base of the epithermal environment. The study further establishes the Galim-Legalgorou prospect as the first well-constrained low-sulfidation epithermal Au–Ag mineralization documented along the Cameroon Volcanic Line, and demonstrates that mantle-derived magmatism in an intracontinental rift system can generate epithermal mineralization comparable to arc-related systems, expanding global models of precious-metal formation in volcanic terranes.

Keywords Whole-rock geochemistry · Microthermometry · Hydrothermal fluid · Boiling · Na–K geothermometry

✉ Terence Cho Ngang
terence.cho@rwth-aachen.de

[1] Department of Geology, Mining and Environmental Science, Faculty of Science, The University of Bamenda, P.O. Box 39, Bambili, North West Region, Cameroon

[2] Institute of Mineralogy and Economic Geology, RWTH Aachen University, Wüllnerstrasse 2, 52062 Aachen, Germany

[3] GFZ Helmholtz Centre for Geosciences, Telegrafenberg, 14473 Potsdam, Germany

[4] Economic Geology Unit, Department of Geology, Faculty of Science, University of Buea, Box 63, Buea, South West Region, Cameroon

[5] Department of Geology, Pan African University Life and Earth Sciences Institute (PAULESI), University of Ibadan, Ibadan, Nigeria

[6] Department of Civil Engineering, The University Institute of Technology (IUT), University of Douala, P. O. Box 8698, Douala, Cameroon

[7] Department of Earth Sciences, University of Yaoundé I, P.O. Box 812, Yaoundé, Cameroon

Published online: 25 June 2026

Introduction

The Galim-Legalgorou area in north-western Cameroon (Fig. 1a) has been shown to host epithermal Au–Ag mineralization linked to Cenozoic volcanic rocks along the Cameroon volcanic line (CVL)—an intracontinental rift system (Ngang et al. 2024). Until very recently, Cameroon was, previously, only known for orogenic gold occurrences hosted within shear zones and quartz veins in Precambrian rocks (Suh et al. 2006; Azeuda Ndonfack et al. 2021a, b). Epithermal deposits can be hosted in volcanic rocks of all ages, although most preserved deposits are linked to Cenozoic volcanic arcs (Hedenquist et al. 2000) associated with a mix of magmatic and meteoric fluids (Sillitoe and Hedenquist 2003). Ore minerals in epithermal systems are known to precipitate from hydrothermal fluids at < 1.5 km depths in response to changes in P–T–X conditions, with key processes being boiling in the up-flow, and mixing on the margins of the system (Taylor 2007).

Studies have demonstrated that the igneous rocks associated with epithermal deposits are characterized by coarse-grained, poorly-sorted breccias, reflecting deposition as debris-flow or block-and-ash deposits from composite volcanoes, most of which appear to be sub-alkaline volcanic rocks of intermediate to acidic composition (du Bray 2017). Studying the host rocks of these deposits usually helps to reveal their nature and unlock the geodynamic environment during mineralization. The volcanic rocks hosting the Galim-Legalgorou Au–Ag Epithermal prospect have not yet been studied.

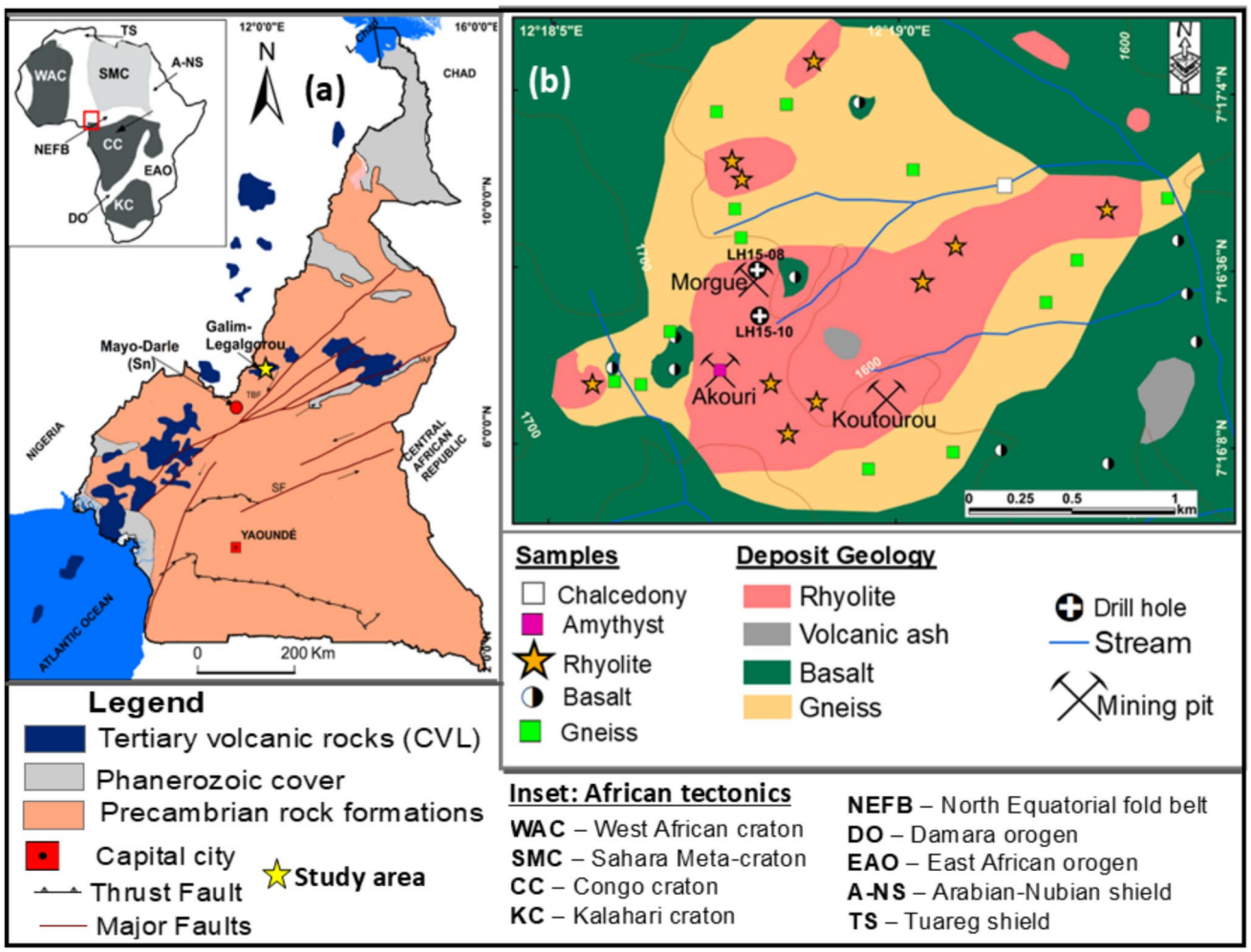

Fig. 1 Geological context of Cameroon and the study area, **a** geology map of Cameroon displaying the volcanic centers of the Cameroon volcanic line (*CVL*), alongside the Tchiolire-Banyo Fault (*TBF*), the Adamwa fault (*AF*), and the Sanaga fault (*SF*), with an inset of major African tectonic terranes. Figure adopted from Ngang et al. (2024). The small arrows represent the sense of displacement along the fault, the yellow star marks the studied area, while the red circle is the location of the area with reported Sn mineralization, **b** sample location map shown on the foreground of the deposit geology

During mineral deposition in epithermal systems, fluid inclusions are trapped in minerals, such as quartz and calcite (Bodnar et al. 1985), and their nature and chemical composition can be unraveled through petrography, microthermometry and chemical analyses of individual fluid inclusions). These mineral systems are usually characterized by low salinity (< 10 wt% $NaCl_{eq.}$) and low temperature (~ 150 to ~ 300 °C) meteoric to magmatic fluids with boiling as, arguably, the main mechanism of mineral deposition, although fluid mixing among fluids of contrasting salinities could be important in some cases (Hedenquist et al. 2000; Taylor 2007). In addition, low porosity and permeability in highly silicified volcanic rocks close to the surface may lead to increased hydrodynamic pressure and compressed isotherms, causing hydraulic fracturing, brecciation and eventual hydrothermal eruptions (Hedenquist et al. 2000; Loucks 2000). This explains the abundant presence of hydrothermal breccia in epithermal deposits. The P–T–X conditions of the Galim-Legalgorou Au–Ag Epithermal prospect have not yet been investigated.

This contribution, therefore, addresses the geochemical character of the host rocks of the Galim-Legalgorou Au–Ag Epithermal prospect, and the nature and composition of fluid inclusions of quartz veins associated with the mineralization, through studies of major and trace elements of host rocks, and petrographic, microthermometric and Raman spectroscopic studies of fluid inclusions. We will discuss the geodynamic and regional implications, the source of magma, processes that triggered mineralization, nature and composition of fluid(s), and compare our data with similar deposit types worldwide.

Geologic and tectonic setting of the Cameroon Volcanic Line

The Cameroon Volcanic Line (CVL) is a prominent geological feature in West and Central Africa, characterized by a chain of tertiary volcanic and plutonic centers extending across the Gulf of Guinea and into the African mainland (Adams 2022). The CVL (Fig. 1a) spans ~ 1600 km, from the island of Annobón in the southwest, through the islands of São Tomé, Príncipe, and Bioko in the Gulf of Guinea, and continues northeastward into the mainland of Cameroon, culminating near Lake Chad. The CVL is geologically significant due to its unusual linear structure and its association with both oceanic and continental volcanism, which presents a unique case for understanding tectonic and magmatic processes in intra-plate settings.

The CVL is classified as a "hotline" volcanic system, distinct from the more commonly known hotspot volcanic chains (Adams 2022). Unlike typical hotspots, such as the Hawaiian-Emperor chain, which result from stationary mantle plumes beneath moving tectonic plates, the CVL does not fit into this model (Bastow et al. 2012). It is instead believed to result from complex interactions between lithospheric fractures and upwelling mantle material, though the exact mechanisms remain debated (Adams 2022). One widely accepted hypothesis suggests that the line may be linked to the reactivation of previous tectonic fractures in the lithosphere, particularly those associated with the opening of the South Atlantic Ocean during the breakup of Gondwana in the Mesozoic era (Fitton 1987; Adams 2022).

Tectonically, the CVL is situated at the intersection of the West African Craton and the Congo Craton, intruding Pan-African Neoproterozoic rocks of the north-western Cameroon domain and the Adamawa-Yade domain (Adams 2022). The emplacement of plutonic and volcanic rocks of the CVL is thought to be directly linked to major pre-Mesozoic tectonic features, such as the Adamawa fault (AF) and the Tchiolire-Banyo fault (TBF), that run parallel to the volcanic centers (Ngako et al. 2008). These tectonic features are believed to have played a significant role in the localization of volcanism along the CVL (Ngako et al. 2008). Some studies suggest that lithospheric thinning and localized mantle upwelling beneath the CVL may have been triggered by extension along these fault zones during the late Cretaceous to early Cenozoic periods (Guiraud and Maurin 1992). The complex geology of the CVL makes it an important natural laboratory for studying intra-plate volcanism, lithospheric dynamics, and the geological evolution of West and Central Africa (Fitton 1987).

Data on the mineral resource potential of the CVL are very limited, with suggestions that there may be prospects of gold, silver, tin and REEs (Lavenir et al. 2023; Tantoh et al. 2024; Ngang et al. 2024). Apart from the recently reported Au–Ag epithermal mineralization at Galim-Legalgorou (Ngang et al. 2024), alkaline ring complexes of upper Cretaceous to Eocene age, consisting of anorogenic granites, quartz-syenites and granite intrusions, host tin deposits, and have been the focus of artisanal mining for more than 100 years in the Mayo-Darle area (Tantoh et al. 2024). The Mayo-Darle prospect potentially holds more than 100 Mt of low-grade cassiterite ore, estimated at 0.1–0.3 wt% SnO_2, hosted by hydrothermal veins, stockworks and greisen that formed at about the same time (~ 54–56 Ma) as the onset of magmatism along the CVL (Nguene 1982; Tantoh et al. 2024).

Local geology and rock types

The main features of the Galim-Legalgorou Au–Ag prospect were first described by Ngang et al. (2024). The main host rocks observed at Galim-Legalgorou are basaltic and rhyolitic units (brecciated and undisturbed), all of which are underlain by a Precambrian basement of ortho-gneisses (Fig. 1b). In brief, the gold mineralization is hosted within

jogs, which are small fractures in brecciated felsic volcanic rocks, that are healed by quartz, pyrite, hematite, goethite and enveloped by halos of hydrothermal alteration (Ngang et al. 2024). Gold occurs as electrum and is associated with pyrite, Fe-rich sphalerite and acanthite.

Basalt occurs as lava flows, with boulders commonly in contact with the rhyolitic units. Three sub-types of basaltic rocks were distinguished in the field. Basalt I (Fig. 2a) has a fine to medium grain texture with pyroxene phenocrysts, is weakly magnetic and dark in color, and occurs mainly as boulders and a few outcrops. Basalt II is a remnant of a volcanic plug, in contact with basalt I and the rhyolitic units. It is dark in color, is moderately magnetic, and has a porphyritic texture with millimeter-sized plagioclase phenocrysts (Fig. 2b). Basalt III occurs as large boulders and in outcrop; the rock is gray and phenocrysts of plagioclase and pyroxenes are present in an equigranular, medium grain texture (Fig. 2c).

Samples of basalt I and II show a porphyritic texture in which large pyroxene (or plagioclase) phenocryst are embedded in a background of much smaller plagioclase/pyroxene crystals, in turn within a fine ground mass (basalt I and II) (Fig. 3a–d). Basalt III shows ophitic to sub-ophitic textures with large plagioclase laths arranged in an irregular fashion around pyroxene crystals of approximately the same size (Fig. 3e, f**).** The mineralogy of basalt I is plagioclase (45–55 vol.%), clinopyroxene (10 vol.%), orthopyroxene (25 vol.%), olivine (< 5 vol.%) and Ti-bearing magnetite (~ 2 vol.%), while basalt II has plagioclase (50–60 vol.%), pyroxene (20–25 vol.%) and Ti-bearing magnetite (Ti-mt) (< 5 vol.%). Large inclusions of clinopyroxene are observed in plagioclase crystals in basalt II (Fig. 3d), indicating that the albite postdates the pyroxenes. Basalt III consists of plagioclase (40–50 vol.%), orthopyroxene (20 vol.%), clinopyroxene (15 vol.%), Ti-mt (about 5 vol.%), olivine (about 5 vol.%) and apatite (< 2 vol.%).

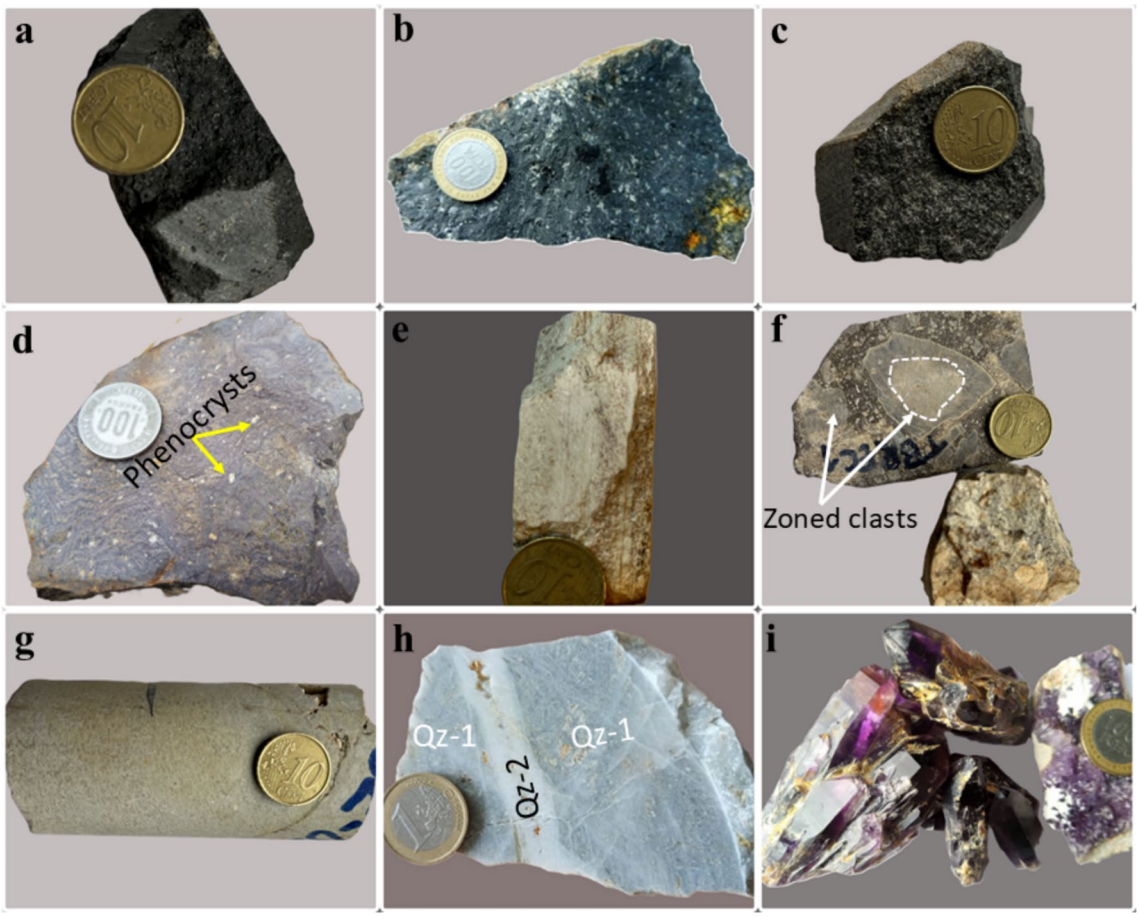

Fig. 2 Representative hand specimen samples of the different volcanic rocks in Galim-legalgorou: **a–c** Grab samples of basalt I, II and III, respectively, **d** trachyte with clearly visible alkali feldspar phenocrysts, **e** grab sample of rhyolite with flow-banding texture, **f** half-core sample of volcanic breccia with zoned angular, felsic clasts, **g** fresh half-core sample of rhyolite, **h** hand specimen sample of two-generational chalcedony vein, Qz-2 postdating Qz-1, **i** Well formed amethyst crystals recovered from artisanal mining pit. Amethyst is more spatially linked to mineralized zones than is chalcedony

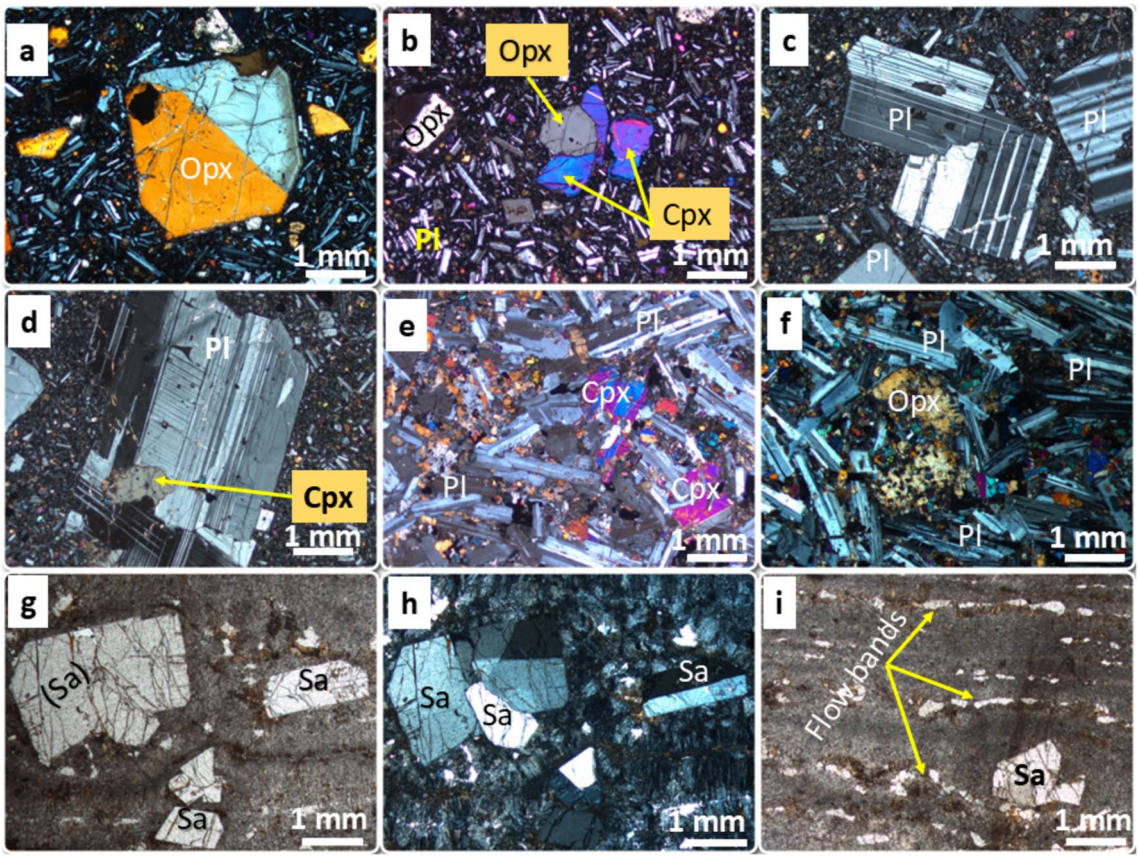

Fig. 3 Representative photomicrographs of the volcanic host rocks, **a**, **b** transmitted light image of basalt I, seen in crossed polarized light (*XPL*). Notice ortho-proxene (*Opx*) growing into clinopyroxene (*Cpx*), indicating coprecipitation, **c**, **d** XPL image of Basalt II showing large blocks of plagioclase (*Pl*) with inclusions of clinopyroxene, **e**, **f** XPL image Basalt III with oophytic textural arrangement of roughly equigrannular crystals of opx and plagioclase laths, **g** large prismatic crystals of sanidine (*Sa*) in (**g**) plane polarized light (*PPL*) and **h** in crossed polarized light. Notice the simple twinning in sanidine and the horizontal extinction angles, **i** Lava flow textures in rhyolite, with alternating sanidine bands (white) in a cryptocrystalline groundmass

Orthopyroxene forms euhedral octagonal crystals which have strongly pitted surfaces, altered rims, a high positive relief and shows a grey to yellow color with a simple twin in cross-polarized light (XPL) (Fig. 3a). The orthopyroxene crystals are commonly intergrown with one another and locally with crystals of clinopyroxene. Clinopyroxene forms fairly elongate crystals, has a weak cleavage and shows a gray color in plane polarized light (PPL) (Fig. 3b). The mineral shows strongly weathered rims and second-order yellow, purple to blue interference colors in crossed polarized light (XPL). Chalcopyrite appears yellow in reflected light, occurs as anhedral grains that are commonly intergrown with Ti-bearing magnetite (Ti-mt) or as inclusions in either plagioclase or pyroxene (Fig. 4a–c). Ti-mt, ≤ 5 vol.%, is white–gray in reflected light and is locally intergrown with clinopyroxene, plagioclase and apatite. Although zircons are not readily observed in polished rock mounts and thin sections, grain mounts of heavy mineral concentrates obtained from crushed mineralized rocks are dominated by zircon grains (Fig. 4d**).** Apatite also exists as an accessory mineral phase (< 1 vol.%) in basalt III. In back-scattered scanning electron photomicrographs (BSE–SEM), apatite occurs as small euhedral elongated crystals, with hexagonal basal sections (Fig. 4e, f), and is commonly intergrown with Ti-mt, suggesting coprecipitation.

Rhyolite occurs as large boulders and in outcrops, as relics of lava flows, and varies in color from white to yellowish brown to grey (Fig. 2d–g). In some places, the rhyolite has a characteristic flow-banding texture (Fig. 2e). The rock is composed principally of K-feldspars (sanidine and orthoclase > 60 vol.%), quartz (< 35 vol.%) and less than 5 vol.% biotite and plagioclase in the groundmass. In plane polarized light (PPL), rhyolite exhibits a banded texture, with alternating bands of sanidine crystals in a cryptocrystalline groundmass (Fig. 3i). Large, randomly oriented phenocrysts of sanidine are also common within the rock matrix. In XPL, sanidine occurs mostly as large monoclinic crystals and

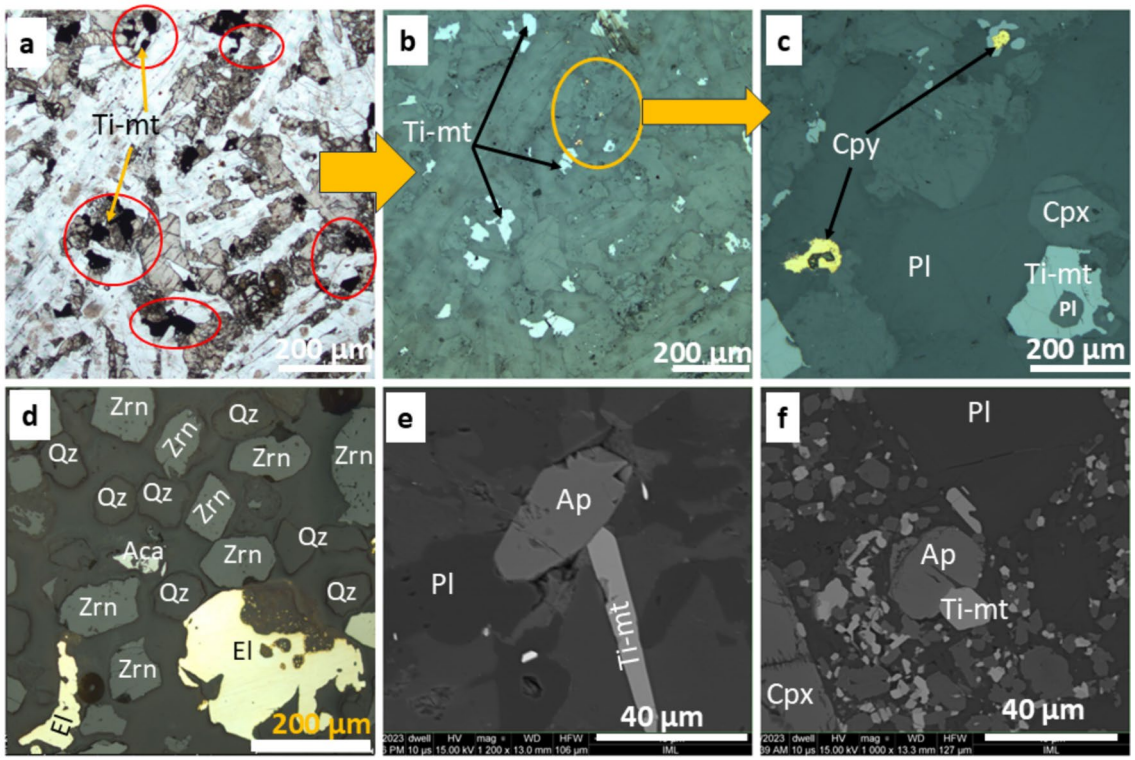

Fig. 4 Photomicrographs and SEM images of basalt III, showing the distribution and petrographic relationships of the accessory mineral phases—titanomagnetite (*Ti-mt*), apatite (*Ap*) and chalcopyrite (*Cpy*) within the rock (**a–c**) distribution of Ti-mt and Cpy shown in reflected light (**d**) Zircon (*Zrn*) crystals in heavy mineral concentrate from crushed mineralized rock samples, shown with quartz (*Qz*) acanthite (*Aca*) and electrum (*El*) (**e**, **f**) Ti-mt and apatite in SEM. Notice intergrowth of apatite and Ti-mt, suggesting coprecipitation

shows simple twinning with horizontal extinction angles in rhyolitic rocks (Fig. 3g, h). It shows no cleavage, although many irregular cracks are common on the surface. Biotite gneiss (Appendix 3–4) constitutes the basement rock in the studied area.

In some cases, rhyolite has been hydrothermally brecciated and mineralized, mainly with disseminations of pyrite. In brief, Au and Ag mineralization occurs as electrum (~ 50:50 wt% composition) within ~ 1–5 cm jogs in the rhyolitic rocks which are variably brecciated and hydrothermally altered (Ngang et al. 2024). Ore mineral associations include pyrite, sphalerite, acanthite, specular hematite and goethite. Kaolinite, dickite, adularia and chlorite/smectite constitute the major alteration phases, while quartz constitutes the main gangue mineral. Quartz occurs as chalcedony (Fig. 2h) and amethyst (Fig. 2i), in quartz veins and ore jogs, with chalcedony having two separate generations, an early generation (Qz-1) that is crossed-cut by a late generation (Qz-2). In the field, gold mineralization appears more closely linked to amethyst than chalcedony.

Field data for all samples and petrographic data for the biotite gneiss are shown in Appendix 1–4.

Sampling and analytical methods

The sampling and analytical methods and procedures employed to obtain the results in this study are detailly outlined in Appendix 5. In summary, field procedures involved careful rock chip sampling from outcrops, boulders and quartz veins as well as selected intervals of core from selected drill holes. Whole-rock major element concentrations were determined by X-ray fluorescence (XRF), while trace elements and REEs were determined by inductively coupled plasma mass spectrometry (ICP-MS) at the Elements and Minerals of the Earth (ElMiE) laboratory, Potsdam, Germany. All other analyses, including Raman spectroscopy for mineral and fluid inclusion analyses, cathodoluminescence for fluid inclusion petrography, laser ablation inductively coupled plasma mass spectrometry (LA-ICP-MS) for fluid inclusion composition, optical microscopy for rock and fluid inclusion petrography, and fluid inclusion

microthermometry were performed at the Institute of Mineralogy and Economic Geology (IML), RWTH Aachen University, Germany.

Results

Whole-rock geochemistry

The full results of whole-rock analysis are shown in Appendix 6. The SiO_2 content of the volcanic rock samples varies from 45.7 wt% to 76.3 wt% and represents a rock suite from basalt and basaltic andesite, to more evolved trachyte and rhyolite units (Fig. 5). The magnesium number (Mg#), 100*Mg/(Mg + Fe), ranges from 27.8 to 38.0 for the basaltic rocks. Statistically significant correlations between different major oxides and silica and the loss on ignition of the lavas are highlighted in Appendix 7.

The Zr and Hf concentrations are higher in the felsic volcanic rocks (average: 40.8 ppm Hf; 1350.0 ppm Zr), relative to the mafic volcanic rocks (average: 4.3 ppm Hf; 212.0 ppm Zr). The rhyolites have a Zr concentrations (1380.0 ppm) that is on average two times higher than that of the trachyte (605.0 ppm). The Zr/Hf ratios range from 13.5 to 41.6 (average 30.1), with one of the basalt samples (BA4) having an outlying value of 113.0. The basalts show higher Sr/Y ratios (average: 30.4) relative to the rhyolites and trachyte (average 0.6). On primitive-mantle normalized spider diagrams (Fig. 6a, b), the basalt, basaltic andesite, trachyte and rhyolite samples show only slight enrichment in large ion lithophile elements (LILE) relative to high field strength elements (HFSE). However, relative depletions are apparent for P, Ti and Y for both sample groups. In addition, the basaltic samples all show significant depletion in K.

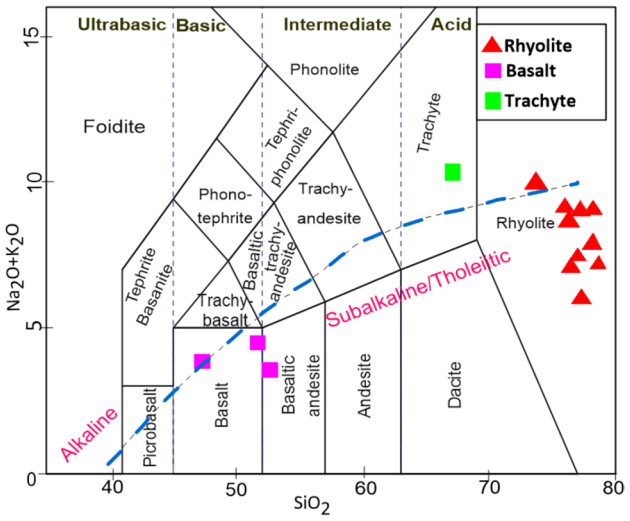

Fig. 5 Total alkali–silica (*TAS*) diagram for the Galim-Legalogou lavas, with compositional boundary from Le Maitre et al. (2002). Most of the samples display a sub-alkaline character with a 'Daly' between 55 and 63% SiO_2

The sum of the REE for the trachyte and rhyolites ranges from 1110 to 1830 ppm (average 1420 ppm), compared to much lower values of 196–559 ppm (average: 540.3 ppm) for the basalts and basaltic andesite. On a chondrite-normalized REE distribution diagram (Fig. 6c), the basalts and basaltic andesite show smooth patterns with enrichments in the light rare-earth elements (LREE) relative to the heavy rare earths (HREE), i.e., the $(La/Yb)_{CN}$ values are in the range of 4.7–12.5 with an average of 9.3. The data show no appreciable Eu anomalies with $(Eu/Eu^*)_{CN}$ in the range of 0.96 to 1.11, with average value of 1.03. However, the basaltic andesite is generally depleted in all REE compared to the basalts, although they have similar REE pattern shapes. On a chondrite-normalized REE spider diagram (Fig. 6b), the rhyolites and trachyte show a slight enrichment in LREE relative to HREE, with $(La/Yb)_{CN}$ ratios of 2.8–9.8 (average: 5.3), and a distinct negative Eu anomaly wth $(Eu/Eu^*)_{CN}$ ratios of 0.09 to 0.51 (average: 0.18).

The basalt and basaltic andesite show variable concentrations of the transition elements Cr (4.8–480 ppm), Sc (18–20 ppm), Co (44–49), Ni (140–170 ppm), V (160–280 ppm) and Cu (21–79 ppm). The basalt and basaltic andesite samples generally have low Ag concentrations (0.53–1.64 ppm), whereas the rhyolites and trachyte have an order of magnitude higher Ag (4.14–24.62 ppm). Silver does not correlate with any of the other trace elements. The transition element signatures of the trachyte and rhyolites show moderate variability for Sc (1.0–24.9 ppm; average: 3.3 ppm), Cr (1.2–5.7 ppm; average: 3.6 ppm), Co (0.1–10.3 ppm; average: 2.2 ppm); Ni (1.1–6.5 ppm; average: 2.4 ppm), Cu (0.5–44 ppm; average: 8.9 ppm) and V (0.3–100 ppm; average: 8.7 ppm). The Ni/Cr ratios range from 0.4 to 5.7 (average: 2.3) for the mafic rocks and from 0.3 to 2.2 (average: 0.8) for the felsic volcanic rocks.

Quartz textures and fluid inclusion types

Superposition of transmitted light and cathodoluminescence (CL) images reveal two stages of quartz growth in amethyst (Q1 and Q2; Fig. 7a–e). Early stage Q1 quartz has Dauphine twinning in CL images, with growth zones developed normal to the twin boundary (Fig. 7c). This early quartz is highly fractured, preferentially along the twin boundaries, parallel to the long (y) axis of the crystal (Fig. 7d). Stage Q2 quartz postdates Q1 and was likely formed by healing of some fractures in Q1. Stage Q2 quartz shows chevron textures with growth zones at acute angles (around 30°) with the twin boundary (Fig. 7e). Growth edges in stage

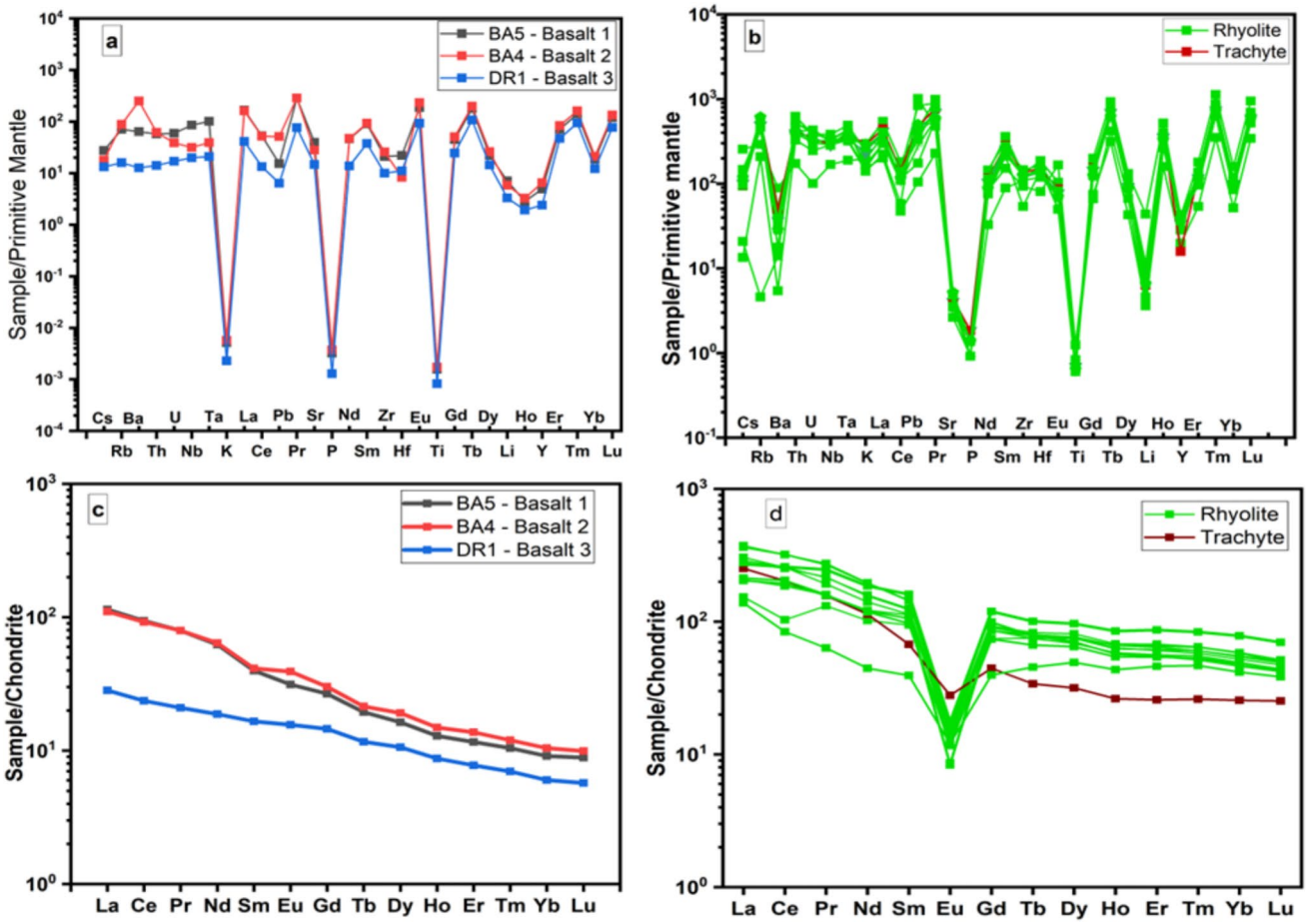

Fig. 6 Trace element spider plots for mafic and felsic units at Galim-Legalgorou: **a** Primitive-mantle normalized multi-element diagrams for basaltic samples and **b** for felsic samples with significant depletion peaks at P, Ti, Y and Ba. **c** Chondrite-normalized REE spider diagrams of basaltic samples showing enrichment of LREE relative to HREE and **d** felsic samples, showing a strong europium anomaly. Data are normalized using values from Sun and McDonough (1989)

Q2 quartz commonly have features indicative of recrystallization. Primary and pseudo-secondary fluid inclusions are associated with growth zones in Q2 quartz, whereas secondary inclusion trails cross-cut both quartz growth stages. Trace element composition of amethyst quartz from Galim-Legalgorou prospect is shown in Appendix 9.

Five sub-types of fluid inclusions (s-type I, s-type II, s-type III, s-type IV and s-type V) were identified in the amethyst samples, based on their occurrence in successive growth zones (stages Q1 and Q2), their morphology and degree of fill (liquid/vapor ratio). All five sub-types are two-phase liquid–vapor (LV type) aqueous fluid inclusions based on their petrographic appearance, with s-type V having highly variable L/V ratios. No three phase aqueous-carbonic fluid inclusions were observed. True primary inclusions with respect to stage Q1 quartz are not present in the samples.

S-type I fluid inclusions are essentially two-phase aqueous (H_2O–NaCl) water-rich inclusions which occur in both primary and pseudo-secondary fluid inclusion assemblages associated with growth zones in stage Q2 amethyst (Fig. 8a–d). These inclusions show round, negative crystal and rice–grain shape and are aligned with growth zones or cross-cut individual but not all growth zones. They range in size from 10 to 50 µm with consistent vapor/liquid ratios between 25 and 30 vol.%.

S-type II fluid inclusions are also liquid-rich inclusions but they are restricted to some growth zones in stage Q2 amethyst quartz. These range in size from 20 to 150 µm and are typically sub-triangular in shape, have vapor/liquid ratios ~ 25 vol.% and may contain a diamond-shaped solid phase (Fig. 8e). This daughter phase is inactive to Raman and does not homogenize into the liquid phase, even at temperatures as high as 400 °C, which rules out that it could be either halite, sylvite, calcite or other carbonate phases.

S-type III fluid inclusions are pseudo-secondary FI trails that cut across growth zones in stage Q2 amethyst. These are elongated in shape and range in size from 20 to 250 µm

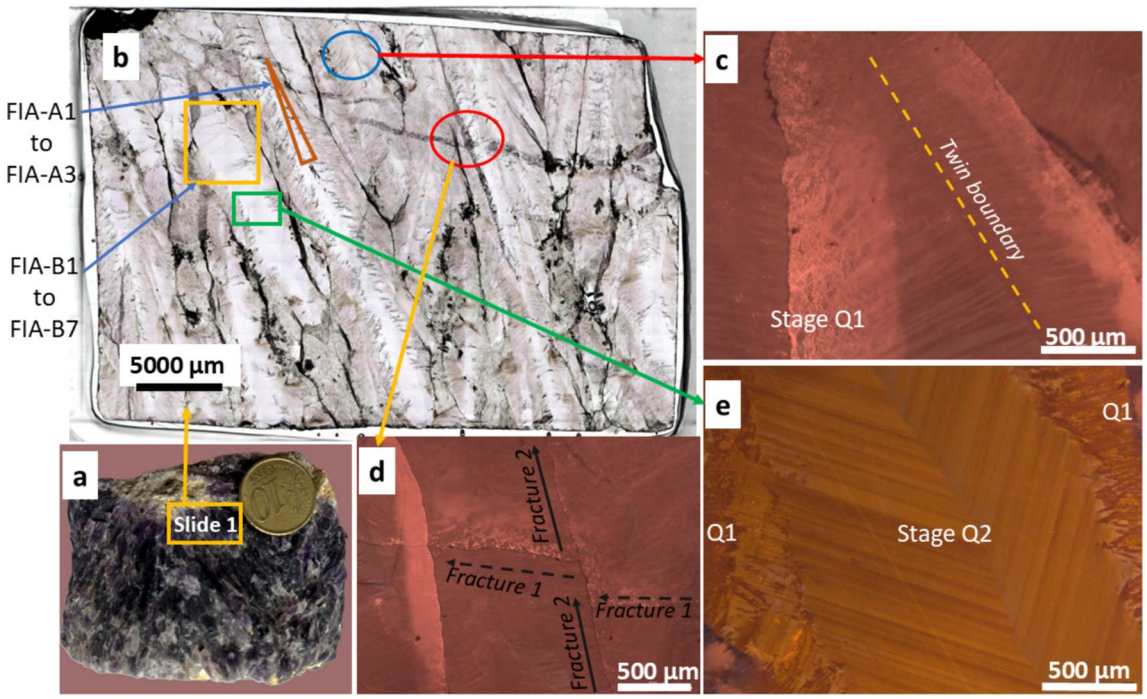

Fig. 7 Textures and internal structures revealed in amethyst quartz **a** amethyst sample with well formed, and moderately fractured individual quartz crystals from Galim-Legalgorou, **b** whole scan of doubly-polished thick section of amethyst sample. Individual quartz crystals slant from top-left to bottom-right and show (in most cases) two stages of quartz growth in brown (early – Q1) and white (late – Q2), **c** hot plate cathodoluminescence (*CL*) image showing stage Q1 quartz growth zone with dauphine twinning, **d** hot plate CL image of healed crossed cutting fractures in amethyst, **e** hot plate CL image showing infilling relationship between Q1 and Q2 (chevron textures) quartz growth stages. Fluid inclusions are mostly associated with stage Q2

(Fig. 8f). The proportion of the vapor phase ranges between 15 to 40 vol.%. Some inclusions show evidence of necking down and contain two optically separate vapor bubbles, that both showed the same Raman signature as other vapor inclusions. Fluid inclusions showing evidence of necking down were not considered further.

S-type IV inclusions are rod-shaped inclusions with sizes ranging from 10 to 30 µm and are aligned with growth zones in stage Q2 amethyst. They have a large range in vapor phase proportions, between < 20 and > 90 vol.% (Fig. 8g).

S-type V inclusions occur in secondary trails that cross-cut growth zones, with co-existing vapor-rich and liquid-rich fluid inclusions with volume ratios of between 0 and 100 vol.% vapor and 0 and 100 vol.% liquid (Fig. 9a–c). Some of these assemblages are almost entirely vapor-rich inclusions (> 90% of the inclusions in a given assemblage), indicating the presence of a vapor phase during fluid evolution.

Microthermometry and fluid inclusion composition

The microthermometric data from this study are summarized in Table 1 and plotted into histograms and bar charts in Fig. 10a, andb. The most abundant, s-type I inclusions, aligned with growth zones in stage Q2 amethyst ($n = 96$) recorded freezing temperatures (T_{frz}) between −34 and −28.5 °C (average −31.3 °C), while those associated with pseudo-secondary assemblages ($n = 23$) froze between −44.5 and −30.5 °C (average −38.4 °C). All s-type I inclusions recorded final ice melting temperatures (Tm_{ice}) between −1.4 and −0.5 °C (average: −1.1 °C). These homogenized (Th) into the liquid phase between 180 and 303 °C (average 273 °C). The salinity of s-type I inclusions was estimated to range from 0.9 to 2.4 wt% $NaCl_{eq}$ (average: 1.8 wt% $NaCl_{eq}$.).

S-type II ($n = 10$) and III inclusions ($n = 15$) showed freezing temperatures between −37.5 and −28.5 °C (average: −30.4 °C) and final ice melting temperatures between −1.8 to −0.8 °C. The calculated salinities are in the range from 1.4 to 3.1 wt% $NaCl_{eq}$. The s-type II inclusions homogenized between 288 and 292 °C (average, 290.4 °C) into the liquid, and s-type III inclusions homogenized between 180 and 262 °C (average, 226 °C) also into the liquid. The solid phase observed in some type s-type II inclusions did not dissolve upon heating, even at temperatures above 360 °C.

Most s-type IV inclusions ($n = 16$) froze at −23.5 to −22.6 °C, and final ice melting occurred at −1.5 to −1.3 °C, corresponding to salinities of 2.1–2.4 wt% $NaCl_{eq}$. These

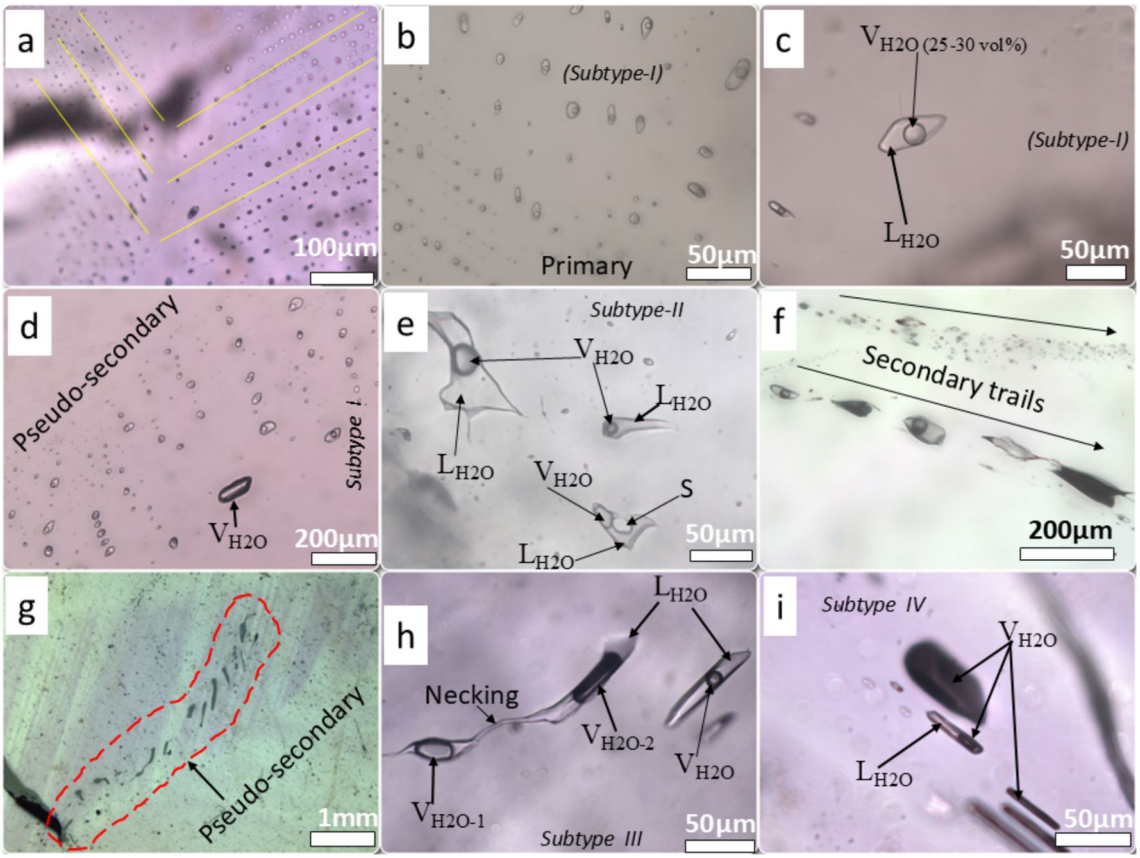

Fig. 8 Fluid inclusion assemblages and inclusion sub-types in amethyst, **a**–**c** primary fluid inclusions (all of sub-type I) along growth zones in stage Q2 quartz, **d** pseudo-secondary inclusions (all of sub-type I) in a planar arrangement in stage Q2 quartz, **e** sub-type II inclusions stage Q2 quartz, **f** Secondary inclusion trails showing evidence of necking, **g**, **h** pseudo-secondary trail of sub-type III inclusions, **i** primary inclusions along Q2 growth zones with gas rich and liquid inclusions of sub-type IV

inclusions homogenize by homogenization of the vapor bubble to liquid at a temperature range between 180 and 245 °C and some became permanently dark immediately after homogenization.

S-type V inclusions ($n = 24$), with coexisting vapor-rich and liquid-rich inclusions, did mostly show freezing between −44.5 and −46 °C with final ice melting temperature between −2.9 and −2.4 °C. This corresponds to a slightly higher salinity of 4.2–4.8 wt% $NaCl_{eq}$., relative to all other inclusion types. These inclusions recorded a wide range of homogenization temperatures of 304–362 °C, due to the large variation in the vapor volume in liquid-rich inclusions (0 to about 100 vol.%).

All inclusions are aqueous only (H_2O–NaCl solution + vapor bubble) based on Raman spectroscopy, which did not show any peaks of additional volatiles, such as CO_2 or CH_4 (Fig. 10c, d). The presence of predominantly water (liquid and vapor) was confirmed by the large and broad peak at Raman wavenumbers around 3000 to 3700 cm^{-1}.

Six inclusions from both primary (to stage Q2 quartz) and pseudo-secondary assemblages were analyzed for their composition by LA-ICP-MS. These were all constant phase L–V s-type I, s-type II and s-type III inclusions. The inclusions show similar chemical compositions with detectable concentrations of Na, K, Cl, Li, B, Fe, As, Rb and Sb. Due to the low salinity, the concentrations of Au, Ag, Cu, Pb and Zn were not detected. Na^+ (average 7280 ppm) and K^+ (average 1803 ppm) are the dominant cations in solution, and Cl^- (14,251 ppm) is the dominating anion (Fig. 10e and Table 2). The mass-based K/Na ratios are in the range of 0.21 to 0.28 (average 0.25).

Discussion

Petrogenesis, magmatic evolution and tectonic setting

Epithermal deposits are mainly driven by calc–alkaline subduction-related and collisional magmatism and to some

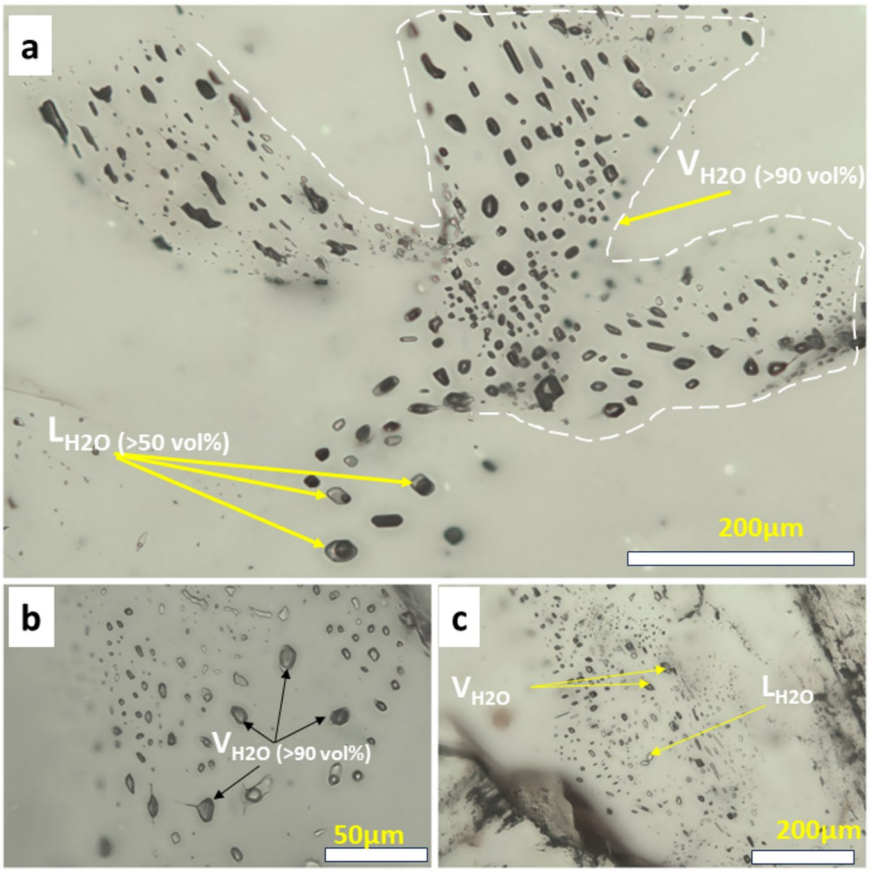

Fig. 9 S-type V fluid inclusions suggestive of effervescence and boiling **a** cross-cutting secondary inclusion trails with majority vapor-rich inclusions (> 70%) coexisting with liquid-rich inclusions, providing evidence of steam exsolution and boiling (?), **b**, **c** co-existing vapor and liquid-rich inclusion assemblages with significant liquid-only inclusions, could also be attributed to post-entrapment modification (necking)

Table 1 Summary of the major fluid inclusion characteristics obtained from FI microthermometry

Properties	FI in Amethyst				
	Sub-type I	*Sub-type II*	*Sub-type III*	*Sub-type IV*	*Sub-type V*
Phase at 25 °C	$L_{H2O}+V_{H2O}$	$L_{H2O}+V_{H2O}$	$L_{H2O}+V_{H2O}$	$L_{H2O}+V_{H2O}$	$L_{H2O}+V_{H2O}$
Inclusion origin	Primary/PS *w.r.t* Q2 quartz	Primary *w.r.t* Q2 quartz	PS *w.r.t* Q2 quartz	Primary *w.r.t* Q2 quartz	Secondary *w.r.t* Q2 quartz
Occurrence	Along chevron growth zones	Cluster within chevron growth zones	Planar arrays of sealed cracks	Along growth zones	Mostly along trails cutting all growth zones
Total inclusions measured	119	10	22	16	24
Size (cm^{-3})	18–48	20–150	20–250	10–30	< 10–250
T_{frz} (°C)	−44 to −28.5	−37.5 to −28.5	−37.5 to −28.5	−23.5 to −22.6	−46 to −30.5
$Tm_{(ice)}$ (°C)	−1.4 to −0.5	−1.8 to −0.8	−1.8 to −0.8	−1.5 to −1.3	−2.9 to −2.4
Salinity (wt% NaCl eqv)	0.9–2.4	1.74–2.4	1.4–3.06	2.1–2.4	4.2–4.8
Th (°C)	180–303 (*n* = *119*)	288–291.5 (*n* = *10*)	180–261.5 (*n* = *22*)	180–245 (*n* = *11*)	304–362 (*n* = *24*)
Density—gcm^{-3}	0.71–0.78	0.74–0.75	0.79–0.86	0.88–0.91	0.65–0.74

PS Pseudo-secondary, *w.r.t* with respect to

extent, to the calc–alkaline to tholeiitic back-arc continental rift-associated magmatism (Siani et al. 2020; du Bray 2017). The distribution of epithermal deposits in subalkaline volcanic rocks are largely associated with rocks of intermediate to acidic composition (andesitic, dacitic and rhyolitic composition), and less commonly so, with basaltic rocks (Bray et al. 2014). The volcanic rocks at the Galim-Legalgorou prospect show a sub-alkaline composition and

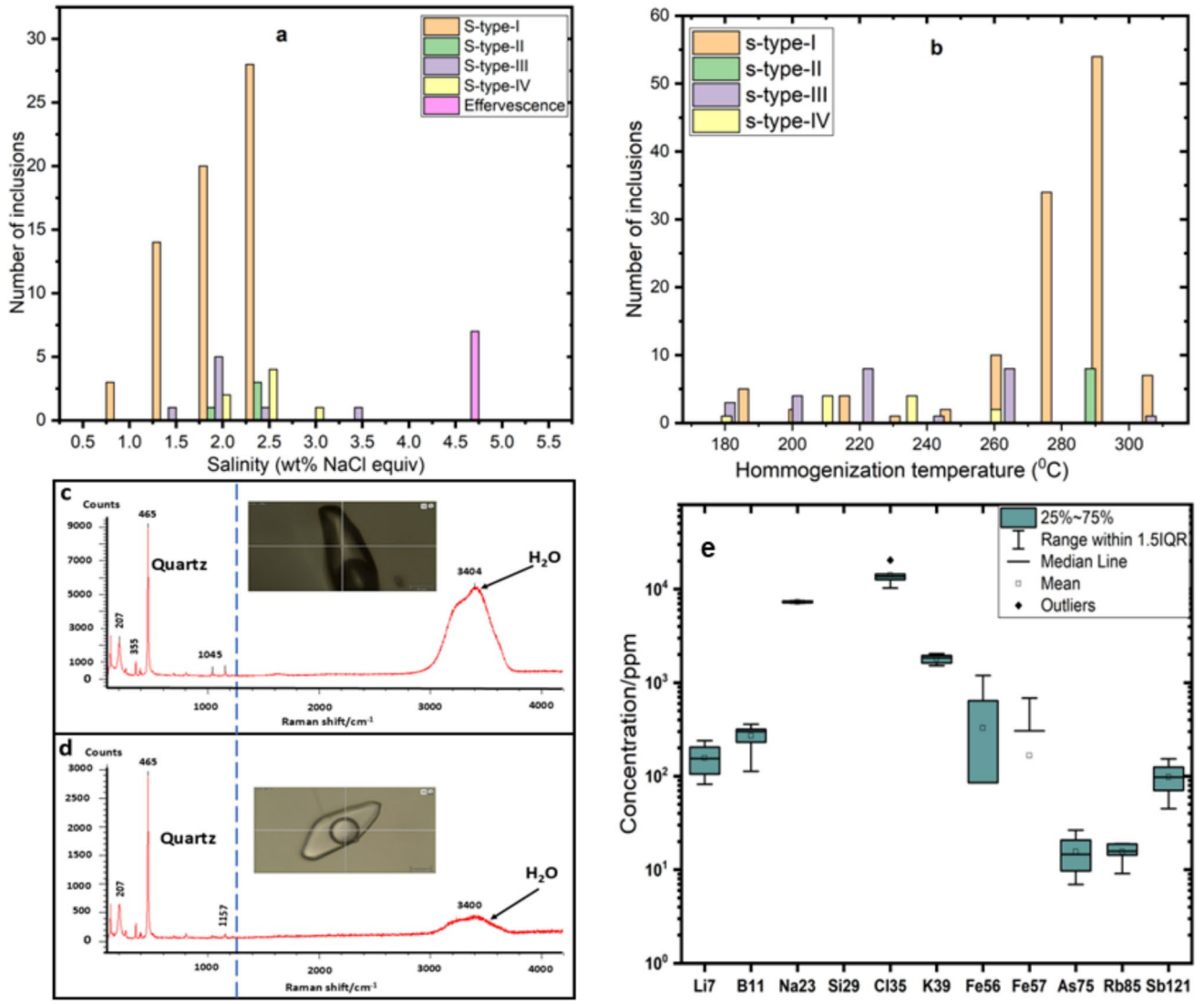

Fig. 10 Representation of microthermometry and composition data for fluid inclusions from Galim-Legalgorou **a** homogenization temperatures and **b** sanity of fluid inclusions measured in amethyst. **c** Laser-Raman spectrographs for liquid and **d** vapor phases for selected inclusions in amethysts, showing that most inclusions are aqueous solutions. The quartz matrix shows characteristic peaks at 465, 207, 1049 and 1157 cm^{-1}, while H_2O (vapor and liquid) are detected at the classical bulge at between 3000 and 3700 cm^{-1} Raman shifts. **e** Box and whisker plot of the concentrations of significant ions in solution. Na and K are most significant cations, with respective concentrations on average of 7280 ppm and 1803 ppm

Table 2 LA-ICP-MS bulk analysis of selected fluid inclusions in amethyst. Concentration is in ppm

Assemblage	Concentration in ppm												
	^{7}Li	^{11}B	^{23}Na	^{24}Mg	^{29}Si	^{35}Cl	^{39}K	^{44}Ca	^{56}Fe	^{57}Fe	^{75}As	^{85}Rb	^{121}Sb
S2_A2	181	358	7126	0	0	12,628	2036	0	170	0	26	19	74
S2_A2	204	315	7107	2	0	13,917	1833	0	0	0	10	17	153
S2_A2	240	284	7258	0	0	10,240	1853	1623	1193	685	7	15	120
S4_A1	127	231	7441	0	0	14,473	1625	0	641	306	21	14	71
S4_A1	105	319	7229	0	0	13,295	1951	0	0	0	15	19	125
S4_A3	82	113	7518	0	0	20,355	1522	0	0	0	15	9	45

< LOD below the limit of detection

range from basalt to rhyolite (Fig. 5), with the rhyolite being the major host, comparable to the general distribution pattern observed in epithermal host rocks in subduction and arc-related settings.

Major oxide components (MgO, CaO, FeO, TiO_2, and Al_2O_3), in the volcanic rocks from the Galim-Legalgorou prospect, typically show a decreasing trend with increasing SiO_2, while K_2O increases with increasing SiO_2, consistent with fractional crystallization in the medium-to-high-K and shoshonitic environments (Siani et al. 2020). The calculated range in Mg# (27.75 to 37.95), together with the bimodality of the lavas, with the so called compositional "Daly" gap between the mafic and the felsic lavas from 52 to 62 wt% SiO_2, indicate that the lavas underwent significant fractionation (Winter 2001), common for CVL lavas (Fitton 1987; Kamgang et al. 2010; Mbassa et al. 2012).

The igneous rock series, as evident in the major element data of this study, comprises rocks of basaltic to rhyolitic composition. According to Asaah et al. (2014), the generation of an igneous series of this character is likely to be the product of magmatic differentiation from a common parent magma or to reflect crustal contamination. Similar major element trends have been reported for felsic volcanic rocks elsewhere on the CVL, such as those from the Bamenda highlands (Kamgang et al. 2010), Manengouba (Kagou Dongmo et al. 2001) and the Tombel graben (Nkouathio et al. 2002). Most epithermal deposits are associated with igneous rocks from sub-alkaline volcanism (Bray et al. 2014, 2017), with intermediate to acidic compositions. The acidic host rocks in this study plot in the calc–alkaline series field on the AFM diagram (Fig. 11b) along the compositional line of Irvine and Baragar (1971), similar to host rocks of epithermal deposits elsewhere in the world (Forsythe et al. 2019).

The systematic trends of some highly incompatible element ratios including Nb/Ta, Sr/Y, Zr/Hf, Ce/Pb, and Nb/U have been shown to be indicators of magmatic fractionation, as they do not change significantly in lavas from the same source (Winter 2001; Asaah et al. 2014). The Nb/Ta ratios in this study vary only slightly (ranging from 13.4 to 17.6), and define a horizontal line on the Nb/Ta vs. SiO_2 variation diagram (Fig. 11a), indicating that both the felsic and mafic lavas were derived from a single highly evolved parental magma (Asaah et al. 2014). Furthermore, with the exception of a single sample (BA4; 113), the Zr/Hf ratios (average 31.6 ± 1.8) of all the lavas vary only slightly within the range of 13.5.1–41.6, suggesting that the lavas were derived from a single magma source, but have undergone significant differentiation (Winter 2001). Although the Zr/Hf ratios are in the range reported for continental volcanic rocks, the absolute concentrations of these elements are anomalously high for the felsic rocks (average values: 1311 ± 265 ppm Zr; 44 ± 7.8 ppm Hf). Due to its high incompatibility, Zr is known to accumulate in the melt phase during magmatic fractionation, especially in magmas with low Zr-saturation limits, leading to the growth and accumulation of zircon crystals that are not easily segregated from the bulk rock (Harrison and Watson 1984). This is supported by the presence of abundant zircon crystals in heavy mineral concentrates from crushed mineralized rocks in this study (Fig. 4d).

Rare-earth element data in mafic rocks and corresponding plagioclase phenocrysts have shown that chondrite-normalized Eu anomalies are caused by the relative stability of divalent europium (Eu^{2+}), relative to other REEs, and are largely controlled by preferential incorporation of Eu^{2+} into plagioclase (Winter 2001). Consequently, the noticeable absence of Eu anomalies in the basalt and basaltic andesite samples in this study may suggest that the melt probably had crystalized much less than 18% plagioclase upon erupting (Philpotts and Schnetzler 1967). By contrast, the trachyte and rhyolites show a pronounced negative Eu anomaly, indicating that plagioclase had strongly fractionated at the magma source, prior to extrusion of the felsic lavas, since Eu is normally incorporated by substitution for Ca into calcic–plagioclase during fractional crystallization. Furthermore, both Sr/Y (average: 7.3 ± 3.9) and $(La/Yb)_N$ (average: 6.08 ± 3.0) are far lower than chondritic values. These data, coupled with the generally elevated concentrations of the REEs and Zr, further suggests a highly fractionated magma originating from low degrees of partial melting, above the garnet stability zone, where plagioclase fractionation peaks (Kelemen and Manning 2015). This signature is consistent with intra-plate and rift volcanic arcs, where magmatism is typically driven by extension-related mantle processes, often involving a relatively undifferentiated mantle source or upwelling from deeper mantle regions with very little crustal contamination. This is, however, not a uniform signature of most lavas on the CVL. In fact, Asaah et al. (2014) reported that the CVL magmas from both the continental and oceanic sectors were generated by small, but different degrees of partial melting of a dominantly garnet–lherzolite mantle, accounting for the minor variations in geochemical characteristics at both local and regional scales. They did, however, recognize that there could be exceptions, especially on the continental sector, given the complex nature of the CVL.

The depletion in P and Ti in the samples of this study is interpreted to be due to their fractionation into apatite and Fe–Ti oxides, respectively. These minerals occur as accessory phases in the mafic rocks. Due to their high mobility, the variable depletion of Ba, Li, and Cs in the trachyte and rhyolite samples on the primitive-mantle normalized spider diagram is probably due to the effect of alteration which affects the more mobile elements at varying degrees (Pandarinath et al. 2007). The high concentrations of Ag in the lavas are interpreted as a direct consequence of

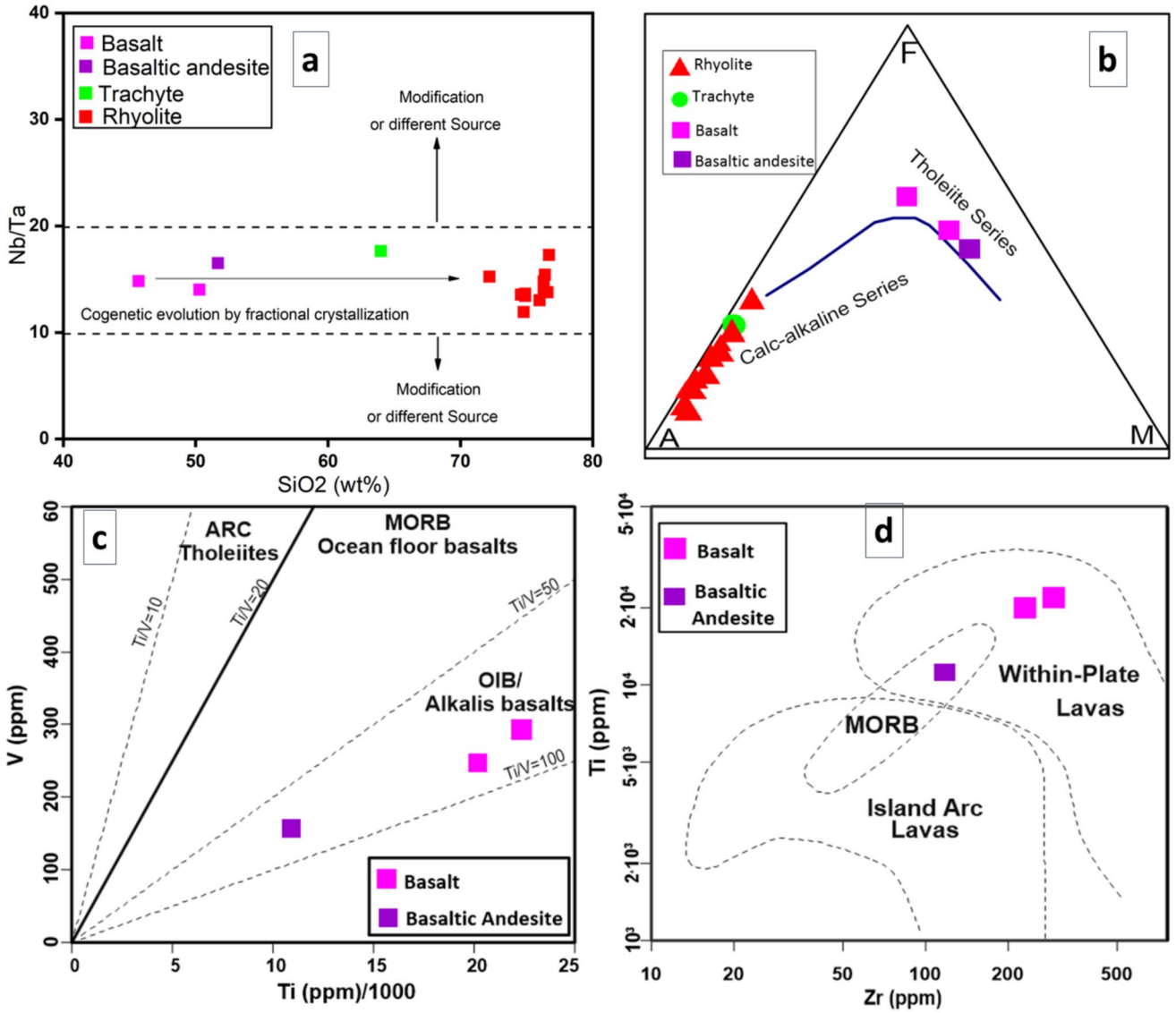

Fig. 11 Discrimination diagrams for the magmatic and tectonic evolution of the CVL based on the lavas from Galim-Legalgorou. **a** SiO_2 vs. Nb/Ta diagram of lavas from Galim-Legalgorou. The samples define a horizontal line, indicating a common magma source, **b** Alkalis–total iron and magnesium (*AFM*) diagram of the same samples in 'a' showing that the rocks define a tholeiitic trend, similar to lavas of OIB origin: The trend line is made after Irvine and Baragar (1971), **c** Ti vs. Zr tectonic discrimination diagram of Pearce (1982). The basalts show a within plate affinity, while the basaltic andesite tends to overlaps with the MORB, **d** V vs. T/1000 discrimination diagram of Shervais (1982), indicating that the Galim-Legalgorou basaltic samples have an OIB affinity

the silicate melt that generated the highly evolved rock series at Galim-Legalgorou. According to Hui et al. (2024), Ag is efficiently transferred to the evolving residual melt during crystallization and crystal melt segregation, and may reach the surface during eruptions. The rhyolites are, therefore, the most likely source of Ag in the Ag-rich electrum reported in an earlier study of this deposit (Ngang et al. 2024). In order to constrain the tectonic environment of magma generation, we have used the Ti–Zr diagram of Pearce (1982) and confirmed this with the V–T/1000 diagram of Shervais (1982). Only the basalt and basaltic andesite samples were used, since they have a more primitive composition close to the parent magma, relative to the trachyte and rhyolites. In the Ti–Zr diagram, the samples plot into the intra-plate lava field (Fig. 11c), although the basaltic andesite overlaps somewhat with the MORB field. The samples also plot in the Ocean Island Basalt (OIB) and Alkali basalt field on the V–T/1000 diagram of Shervais (1982) (Fig. 11d).

In addition to enrichment in REEs and immobile trace elements, highly evolved melts have high concentrations of

water and other volatiles. As the melt ascends through the thin crust in arc settings, the decrease in pressure causes the volatiles in the melt to exsolve, resulting in the formation of hydrothermal fluids. The modification of these fluids through water–rock interactions, fluid mixing, and fluid boiling are the key processes that drive the formation of epithermal mineral deposits in the shallow subsurface (Sillitoe 1993).

The biotite gneiss sample plots in the granodiorite field of the TAS diagram (Cox et al. 1979), implying an I-type granodioritic protolith for the gneiss (Appendix 8). It has an aluminum saturation index (ASI), i.e., molar (Al_2O_3/$CaO + Na_2O + K_2O$) ratio, of 1.0, although molar Al_2O_3 (0.105) is slightly higher than molar of $K_2O + Na_2O$ (0.09). This implies that the biotite gneiss has both weak peraluminous and metaluminous characteristics.

Mineralization temperature, pressure and environment of ore deposition

The petrographic evidence suggestive of boiling indicates that no pressure correction is required (Bodnar et al. 1985; Zhai et al. 2009) and the homogenization conditions are considered to be proxies to the trapping conditions. Only fluid inclusions from s-types I and II, II and III, which make up a majority of the inclusions measured, with fairly consistent properties (L/V filling ratios and Th) were used to make pressure estimates. For the minimum (180 °C) and maximum (303 °C) trapping temperatures, at an average salinity of 2.2 wt% $NaCl_{eq}$, a first estimation of minimum and maximum trapping pressures of 10 bars and 89 bars, respectively, can be made. However, since there exists also evidence of heterogeneous trapping of liquid and vapor, we examined other independent geothermometers such as Na–K, Na–Li and silica thermometers for comparison.

Geothermal systems are comparable to epithermal ore fluids (Henley and Ellis 1983). For a hydrothermal reservoir in equilibrium with Na- and K-rich minerals, the temperature may be estimated using solute thermometry, a method commonly applied in geothermal reservoir exploration. There are several solute thermometers, including the Na–K (Truesdell 1976; Fournier 1979), Na–Li (Fouillac and Michard 1981) and the silica geothermometers. The Na–K thermometer, based on the K/Na ratio in the liquid, is not affected by processes, such as fluid boiling or mixing.

Na–K geothermometry calculations based on the Na/K ratios measured from fluid inclusions with LA-ICP-MS indicate a temperature range between 294 and 328 [average 309 ± 18 °C; other calibrations for this thermometer fall within these two ranges (Table 3)]. This temperature range overlaps the higher end of the range obtained from microthermometry of non-boiling fluid inclusion assemblages in amethyst (up to 303 °C). These two datasets, therefore, suggest that the temperature of the initial mineralizing fluid was about 300 °C at the Galim-Legalgorou prospect. The Na–Li thermometer yields similar to somewhat higher (up to 100 °C) results (Fouillac and Michard 1981) than the Na–K thermometer (Table 3); since the Li content measured is an order of magnitude or more, lower than the K and Na concentrations, the measurement errors will have a large effect on the calculated temperature, and for this reason we

Table 3 Calculated temperatures from various geothermometers using LA-ICP-MS data

Geothermometer	Temperature (°C)						Calibration reference
	S2_A2	S2_A2	S2_A2	S4_A1	S4_A1	S4_A3	
Na–K	315	303	302	286	308	278	Arnorsson et al. (1983)
	323	308	306	285	314	276	Arnorsson (2000)
	322	308	307	287	315	277	Can (2002)
	333	321	320	303	326	296	Giggenbach (1988)
	327	314	313	295	320	286	Fournier (1979)
	351	330	328	298	339	284	Fournier and Truesdell (1973)
	312	299	298	280	305	271	Nieva and Nieva (1987)
	356	336	334	305	344	292	Tonani (1980)
	337	319	317	290	327	278	Truesdell (1976)
	324	312	311	293	317	285	Verma and Santoyo (1997)
Na–Li	414	440	472	342	316	275	Fouillac and Michard (1981)
	419	445	475	349	323	284	Verma and Santoyo (1997)
	397	412	430	351	334	307	Kharaka et al. (1982)
Summary statistics for the Na–K thermometer							
Mean	330	315	314	292	322	282	
Std Dev	14	11	11	8	12	7	
Max	356	336	334	305	344	296	
Min	312	299	298	280	305	271	

prefer the Na/K geothermeter results. Overall, the results are consistent with the deep reservoir fluid buffered by cation-exchange equilibria (Xilai et al. 2002).

The fluid inclusion data, in combination with the field relations are useful proxies for the environment of ore deposition. The homogenization temperature vs. the fluid salinity of the Galim-Legalgorou prospect, < 300 °C and < 3 wt% $NaCl_{eq}$., is typical of epithermal Au–Ag deposits (Wilkinson 2001), supported by the Fe-rich sphalerite in the deposit noted by Ngang et al. (2024), is consistent with the Galim-Legalgorou deposit as having a low-sulfidation affiliation, based on the characteristic features noted by Sillitoe and Hedenquist (2003).

Mechanisms of ore deposition

Most fluid inclusions (s-type I to s-type IV) in this study contain only two phases at room temperature (aqueous liquid and vapor) and have generally low salinities (< 5 wt% $NaCl_{eq}$.) and homogenization temperatures between 180 and 303 °C. These characteristics are typical of fluid inclusions trapped in the epithermal environment (Bodnar et al. 1985; Sillitoe and Hedenquist 2003). The rather wide range in homogenization temperatures suggests that the fluid system may have undergone transient periods of hydrostatic fluid pressure with different degrees of boiling (Zhai et al. 2009; Azeuda Ndonfack et al. 2021a, b). These fluctuations are indicated by the complex growth zoning and the different generations of quartz veins observed in the field and are also recorded by the texturally and chemically zoned electrum grains reported by Ngang et al. (2024).

Epithermal mineral deposits are broadly considered to be formed from mixtures of meteoric and magmatic–hydrothermal fluids (Hedenquist et al. 2000). The dominance of Na^+ and K^+, relative to other fluid components, is a function of fluid equilibrium with Na- and K-rich minerals at the time of mineralization at Galim-Legalgorou.

The observation of FIAs with coexisting vapor-rich and liquid-rich inclusions leads to the conclusion that boiling played an important role in ore deposition. Some inclusions (Fig. 9b, c) have been affected by necking down, following the entrapment of the inclusion, and the presence of numerous liquid-only inclusions in the assemblage is also likely the product of necking down (Bodnar et al. 1985; Bodnar 2003). However, some vapor-rich inclusions in cross-cutting micro-fractures (Fig. 9a) indicate that a separate vapor phase likely formed in the system due to boiling. Boiling is considered to be the main factor leading to precipitation and enrichment of gold and silver in epithermal deposits, with abundant evidence in many epithermal gold deposits, such as Hishikari, Japan (Faure et al. 2002), Mule Canyon, Nevada, USA (John et al. 2003) and Golden Cross, New Zealand (Simpson et al. 2001). However, while most of these deposits are associated with calc–alkaline, subduction-related arc magmatic systems, Galim-Legalgorou occurs within an intra-plate rift system, a unique feature, making it a major offset to current epithermal deposit models and a geological attraction for modern epithermal systems research (Ngang et al. 2024).

A negative correlation is observed between homogenization temperatures and fluid salinities (Fig. 12), possibly indicating an apparent increase in salinity and cooling of the liquid phase due to the loss of H_2O vapor; the nature of these trends precludes mixing between hydrothermal solution and groundwater (Zhai et al. 2009). This indicates that the low-salinity ore-forming fluids at Galim-Legalgorou boiled during mineralization.

Conclusion

The whole-rock composition and fluid inclusion data presented in this work complement earlier mineralogical and microchemical studies of the Galim-Legalgorou Au–Ag prospect. While the whole-rock compositions show similar characteristics to those of host volcanic rocks associated with epithermal Au–Ag deposits in other parts of the world, the fluid inclusion data suggest that the epithermal Au–Ag mineralization formed in at least two successive hydrothermal stages at typical epithermal temperatures

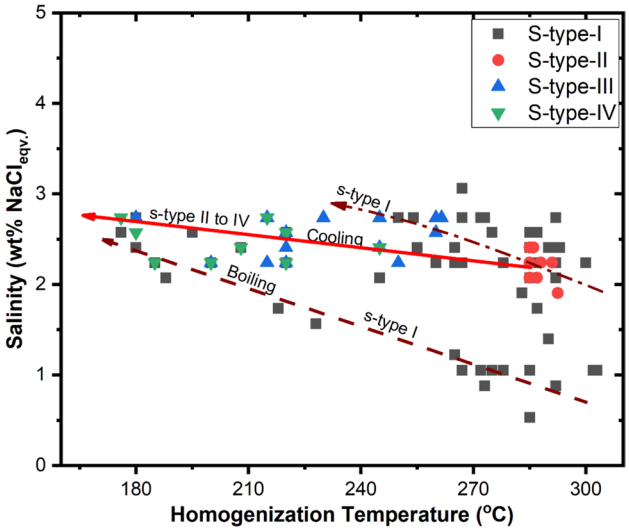

Fig. 12 Plot of salinity vs. homogenization temperatures of fluid inclusions, showing the path of fluid evolution in Galim-Legalgorou Ag–Au mineralization. The general trend of increasing salinity with decreasing temperature is suggestive of cooling from boiling. No positive trend is observed in any inclusion sub-type, ruling out the role of mixing of fluids of contrasting salinities in the mineralization process

(about 300 °C). These data, in addition to the ore mineral associations, mineral compositions of electrum and sphalerite and hydrothermal alteration signatures reported in an earlier study, justify the conclusion that the Galim-Legalgorou prospect represents a low-sulfidation epithermal system. The recognition of a low-sulfidation epithermal Au–Ag system along the CVL demonstrates that significant precious-metal mineralization can develop in intra-plate, rift-related magmatic environments—settings that remain poorly represented in global metallogenic models. This finding expands the global framework for epithermal metallogeny beyond subduction-arc terranes and positions the CVL as a promising frontier for future exploration and comparative epithermal research.

Supplementary Information The online version contains supplementary material available at https://doi.org/10.1007/s00531-026-02593-8.

Acknowledgements This publication is part of the PhD thesis of the first author. Funding for a 2-year research stay at the Institute of Mineralogy and Economic Geology (IML), RWTH Aachen University, in Germany was awarded by the German Academic Exchange Service (DAAD) within the framework of the bi-nationally supervised doctorate scholarship program. The management of Daewoo International Cameroon S.A. is also acknowledged for providing fresh mineralized core samples for this study. This study was also supported by the German Research Foundation (DFG), infrastructure grant INST222/1401-1. Comprehensive reviews from Jeffery Hedenquist (reviewer #1), one anonymous person (reviewer #2) and the topic editor of the International Journal of Earh Sciences (IJES), Peter Lightfoot, contributed immensely to improving this publication.

Funding Open Access funding enabled and organized by Projekt DEAL. This study was funded by German Academic Exchange Service, 57588368, Terence Cho Ngang.

Data Availability All data used in this work is presented either in form of tables and figures or in the electronic supplementary material section.

Declarations

Conflict of interest The author(s) declare no competing interest.

References

Adams A (2022) Insights into the source of magmatic hot-lines: forty years of geophysical studies of the Cameroon Volcanic Line. Front Earth Sci 10:838993. https://doi.org/10.3389/feart.2022.838993

Arnorsson S (2000) Isotopic and chemical techniques in geothermal exploration, development and use: sampling methods, data handling, interpretation. International Atomic Energy Agency, Vienna, p 351

Arnorsson S, Gunnlaugsson E, Svavarsson H (1983) The chemistry of geothermal waters in Iceland-II. Mineral equilibria and independent variables controlling water compositions. Geochim Cosmochim Acta 47:547–566

Asaah ANE, Yokoyama T, Aka FT, Usui T, Wirmvem MJ, Tchamabe BC, Ohba T, Tanyileke G, Hell JV (2014) A comparative review of petrogenetic processes beneath the Cameroon Volcanic Line: geochemical constraints. Geosci Front 6:557–570. https://doi.org/10.1016/j.gsf.2014.04.012

Azeuda Ndonfack KI, Xie Y, Goldfarb R (2021a) Gold occurrences of the Woumbou–Colomine–Kette District, eastern Cameroon: ore-forming constraints from petrography, SEM–CL imagery, fluid inclusions, and C–O–H–S isotopes. Miner Deposita 57:83–105. https://doi.org/10.1007/s00126-021-01050-7

Azeuda Ndonfack KI, Xie Y, Goldfarb R, Zhong R, Qu Y (2021b) Genesis and mineralization style of gold occurrences of the Lower Lom Belt, Bétaré Oya District, eastern Cameroon. Ore Geol Rev 139:104586. https://doi.org/10.1016/j.oregeorev.2021.104586

Bastow I, De Plaen R, Gallacher R (2012) The development of the Cameroon Volcanic Line: Evidence from seismic anisotropy and receiver functions. Department of Earth Sciences, University of Bristol, BS8 1RJ, UK. https://www.researchgate.net/publication/258615654

Bodnar RJ (2003) Re-equilibration of fluid inclusions. In: Samson I, Anderson A, Marshall D (eds) Fluid inclusions: analysis and interpretation. Mineral. Assoc. Canada, Short Course 32, 213–230

Bodnar RJ, Reynolds TJ, Kuehn CA (1985) Fluid inclusion systematics in epithermal systems. In: Berger BR, Bethke PM (eds) Geology and geochemistry of epithermal systems. Reviews in Economic Geology, 1985/01/01; pp 73–97

Bongiovanni M, Fusswinkel T, Marks MAW (2024) Unravelling the effects of magmatic fractionation, fluid phase separation and dilution on the composition of magmatic-hydrothermal fluids of the Cornubian Batholith (SW England). Chem Geol 658:122119. https://doi.org/10.1016/j.chemgeo.2024.122119

Can I (2002) A new improved Na/K geothermometer by artificial neural networks. Geothermics 31:751–760

du Bray EA (2017) Geochemical characteristics of igneous rocks associated with epithermal mineral deposits—a review. Ore Geol Rev 80:767–783. https://doi.org/10.1016/j.oregeorev.2016.08.023. (**ISSN 0169-1368**)

du Bray EA, John DA, Cousens BL (2014) Petrologic, tectonic, and metallogenic evolution of the southern segment of the ancestral Cascades Magmatic Arc, California and Nevada. Geosphere 10:1–39. https://doi.org/10.1130/GES00944.1

Faure K, Matsuhisa Y, Metsugi H, Mizota C, Hayashi S (2002) The Hishikari Au–Ag epithermal deposit, Japan: oxygen and hydrogen isotope evidence in determining the source of paleohydrothermal fluids. Econ Geol 97:481–498

Fitton JG (1987) The Cameroon Line, West Africa: a comparison between oceanic and continental alkaline volcanism. In: Fitton JG, Upton BGJ (eds) Alkaline igneous rocks. Geological Society, London, pp 273–291

Forsythe NA, Spry PG, Thompson ML (2019) Petrological and mineralogical aspects of epithermal low-sulfidation Au- and porphyry

Cu-style mineralization, Navilawa Caldera, Fiji. Geosciences (Basel) 9(1):42. https://doi.org/10.3390/geosciences9010042
Fouillac C, Michard G (1981) Sodium/lithium ratio in water applied to geothermometry of geothermal reservoirs. Geothermics 10:55–70
Fournier RO (1979) A revised equation for the Na/K geothermometer. Geotherm Res Counc Trans 3:221–224
Fournier RO, Truesdell AH (1973) An empirical Na-K-Ca geothermometer for natural waters. Geochim Cosmochim Acta 37(5):1255–1275
Fusswinkel T, Giehl C, Beermann O, Fredriksson JR, Garbe-Schönberg D, Scholten L, Wagner T (2018) Combined LA-ICP-MS microanalysis of iodine, bromine and chlorine in fluid inclusions. J Anal at Spectrom 33:768–783. https://doi.org/10.1039/c7ja00415j
Giggenbach WF (1988) Geothermal solute equilibria. Derivation of Na-K-Mg-Ca geoindicators. Geochim Cosmochim Acta 52:2749–2765
González-Esvertita E, Fusswinkel T, Canals A, Casase JM, Neilson J, Wagner T, Gomez-Rivasa E (2025) Fluid evolution and halogen fractionation in orogenic belts: a comparative fluid inclusion appraisal in the Eastern Pyrenees. Chem Geol 122578:2025
Guillong M, Meier DL, Allan MM, Heinrich CA, Yardley BW (2008) SILLS: a MATLAB-based program for the reduction of laser ablation ICP-MS data of homogeneous materials and inclusions. Mineral Assoc Can Short Course 40:328–333
Guiraud R, Maurin JC (1992) Early Cretaceous rifts of Western and Central Africa: an overview. Tectonophysics 213(1–2):153–168
Harrison TM, Watson EB (1984) Zircon saturation in magmas. Geochim Cosmochim Acta 48(8):1467–1477
Hedenquist JW, Arribas A, Gonzalez-Urien E (2000) Epithermal gold deposits: styles, characteristics and exploration. Econ Geol 95(3):451–484
Henley RW, Ellis AJ (1983) Geothermal systems ancient and modern: a geochemical review. Earth-Sci Rev 19:1–50
Hui K, Rottier B, Qin K, Zajacz Z, Tsay A, Zhao J, Gao S, Shi R (2024) Silver behavior during magmatic and magmatic hydrothermal evolution of highly evolved reduced granitic system related to the giant Shuangjianzishan Ag-Pb-Zn-(Sn) epithermal deposit, Northeast China. Econ Geol 119(1):59–83. https://doi.org/10.5382/econgeo.5031
Irvine TN, Baragar WRA (1971) A guide to the chemical classification of common volcanic rocks. Can J Earth Sci 8:523–548. https://doi.org/10.1139/e71-055
John DA, Hofstra AH, Fleck RE, Brummer JE, Saderholm EC (2003) Geological setting and genesis of the Mule Canyon low-sulfidation epithermal gold–silver deposit, north-central Nevada. Econ Geol 98:425–463
Kagou Dongmo A, Wandji P, Pouclet A, Vicat JP, Cheilletz A, Nkouathio DG, Alexandrov P, Tchoua FM (2001) Evolution volcanologique du mont Manengouba (Ligne du Cameroun), nouvelles données pétrographiques, géochimiques et géochronologiques. C R Acad Sci, IIA 333:155–162
Kamgang P, Njonfang E, Nono A, Dedzo MG, Tchoua FM (2010) Petrogenesis of a silicic magma system: geochemical evidence from Bamenda Mountains NW Cameroon, Cameroon Volcanic Line. J Afr Earth Sci 58(2):285–304
Kelemen PB, Manning CE (2015) Mantle metasomatism and origin of the Earth's continental crust. Earth Planet Sci Lett 409:44–58. https://doi.org/10.1016/j.epsl.2014.10.055
Kharaka YK, Lico MS and Law LM (1982) Chemical geothermometers applied to formation waters, Gulf of Mexico and California basins (abst.). American Association of Petroleum Geologists Bulletin 66:588
Lavenir NMJ, Fuh NE, Junior EEM (2023) Petrogenesis of the Mayo-Darley tin formations, anorogenic complex of the Cameroon Line: implication for tin deposit. Acta Geochim 42:704–725. https://doi.org/10.1007/s11631-023-00615-9
Loucks RR (2000) Precise geothermometry on fluid inclusion populations that trapped mixtures of immiscible fluids. Am J Sci 300(1):23–59. https://doi.org/10.2475/ajs.300.1.23
Le Maitre RW, Streckeisen A, Zanettin B, Le Bas MJ, Bonin B, Bateman P, Bellieni G, Dudek A, Efremova S, Keller J, Lamere J, Sabine PA, Schmid R, Sorensen H, Woolley AR (2002) Igneous rocks: a classification and glossary of terms, recommendations of the international union of geological sciences, subcommission of the systematics of igneous rocks. Cambridge University Press. ISBN 0-521-66215-X
Mbassa BJ, Njonfang E, Benoit M et al (2012) Mineralogy, geochemistry and petrogenesis of the recent magmatic formations from Mbengwi, a continental sector of the Cameroon Volcanic Line (CVL), Central Africa. Miner Petrol 106:217–242. https://doi.org/10.1007/s00710-012-0227-5
Nieva D and Nieva R (1987) Developments in Geothermal energy in Mexico, part 12: A cationic geothermometer for prospecting of geothermal resources. Heat recovery systems and CHP, 7:243–258
Ngako V, Affaton P, Njonfang E (2008) Pan-African tectonics in northwestern Cameroon: implication for the history of western Gondwana. Gondwana Res 14(3):509–522. https://doi.org/10.1016/j.gr.2008.02.002. (**ISSN 1342-937X**)
Ngang TC, Suh CE, Wagner T, Bafon TG, Fusswinkel T, Vishiti A (2024) Epithermal Ag–Au mineralization at Galim-Legalgorou, Cameroon Volcanic Line: insights from alteration mineralogy and mineral chemistry of electrum and sphalerite. Int J Earth Sci 113:1285–1301. https://doi.org/10.1007/s00531-024-02427-5
Nguene FR (1982) Geology and geochemistry of the Mayo Darle Tin deposit, West central Cameroun, Central Africa. Ph.D. Thesis, New Mexico, Instit of Min. and Techn. Socorro, New Mexico
Nkouathio DG, Ménard JJ, Wandji P, Bardintzeff JM (2002) The Tombel graben (West Cameroon): a recent monogenetic volcanic field of the Cameroon Line. J Afr Earth Sci 35:285–300
Pandarinath K, Dulski P, Torres-Alvarado IS, Verma SP (2007) Element mobility during the hydrothermal alteration of rhyolitic rocks of the Los Azufres geothermal field, Mexico. Geothermics 37(1):53–72. https://doi.org/10.1016/j.geothermics.2007.10.002
Pearce JA (1982) Trace element characteristics of lavas from destructive plate boundaries. In: Thorpe RS (ed) Andesites: orogenic andesites and related rocks. Wiley, pp 252–548
Philpotts JA, Schnetzler CC (1967) Europium anomalies and the genesis of basalt. Chem Geol 3(1):5–13. https://doi.org/10.1016/0009-2541(68)90009-0
Shervais JW (1982) Ti-V plots and the petrogenesis of modern and ophiolitic lavas. Earth Planet Sci Lett 59:101–118. https://doi.org/10.1016/0012-821X(82)90120-0
Siani MG, Lentz DR, Nazarian M (2020) Geochemistry of igneous rocks associated with mineral deposits in the Tarom-Hashtjin metallogenic province, NW Iran: An analysis of the controls on epithermal and related porphyry-style mineralization. Ore Geol Rev 126:103753 (**ISSN 01691368**)
Sillitoe RH (1993) Epithermal models: introduction and overview. Soc Econ Geol Spec Publ 2:1–12
Sillitoe RH, Hedenquist JW (2003) Linkages between volcano-tectonic settings, ore-fluid compositions, and epithermal precious metal deposits. Society of Economic Geologists Special Publications, No. 10, 315–343
Simpson MP, Simmons SF, Mauk JL (2001) Hydrothermal alteration and hydrologic evolution of the golden cross epithermal Au–Ag deposit, New Zealand. Econ Geol 96:773–796
Steele-MacInnis N, Lecumberri-Sanchez P, Bodnar RJ (2012) HOKIEFLINCS_H2O-NACL: a Microsoft excel spreadsheet for interpreting microthermometric data from fluid inclusions based on

the PVTX properties of H2O–NaCl. Comput Geosci 49:334–337. https://doi.org/10.1016/j.cageo.2012.01.022

Suh CE, Lehmann B, Mafany GT (2006) Geology and geochemical aspects of lode gold mineralization at Dimako-Mboscorro, SE Cameroon. Geochem Explor Environ Anal 6:295–309

Tantoh SB, Lehmann B, Suh CE, Ngatcha RB, Zhang R, Cottle J, Nwamba MN, Belyatsky BV, Goldmann S (2024) Zircon and cassiterite U-Pb geochronology and petrochemical characteristics of early Tertiary tin mineralization at Mayo Darlé, Cameroon Volcanic Line. J Geochem Explor 257:107369. https://doi.org/10.1016/j.gexplo.2023.107369

Taylor BE (2007) Epithermal gold deposits. In: Goodfellow WD (ed) Mineral deposits of Canada: a synthesis of major deposit-types, District Metallogeny, The Evolution of Geological Provinces, and Exploration Methods: Geological Association of Canada, Mineral Deposits Division, Special Publication No. 5, pp 113–139

Tonani F (1980) Some remarks on the application of geochemical techniques in geothermal exploration. In: Proceedings of 2nd symposium advances in european geothermal research, Strasbourg, France, pp 428–443

Truesdell AH (1976) Summary of section III. Geochemical techniques in exploration. In: Proceedings of the 2nd United Nations symposium on the development and use of geothermal resources, San Francisco, pp 3–29

Verma SP, Santoyo E (1997) New improved equations for Na/K, Na/Li and SiO_2 geothermometers by outlier detection and rejection. J Volcanol Geotherm Res 79:9–23

Wilkinson JJ (2001) Fluid inclusions in hydrothermal ore deposits. Lithos 55(2001):229–272

Winter JD (2001) An introduction to igneous and metamorphic petrology. Prentice Hall. ISBN 0-13-240342-0. QE461.W735 2001

Xilai Z, Armannsson H, Yongle L, Hanxue Q (2002) Chemical equilibria of thermal waters for the application of geothermometers from the Guanzhong basin, China. J Volcanol Geotherm Res 113(1–2):119–127. https://doi.org/10.1016/S0377-0273(01)00255-4

Zhai W, Sun X, Sun W, Su L, He X, Wu Y (2009) Geology, geochemistry, and genesis of Axi: a Paleozoic low-sulfidation type epithermal gold deposit in Xinjiang, China. Ore Geol Rev 36(4):265–281. https://doi.org/10.1016/j.oregeorev.2009.04.003. (**ISSN 0169-1368**)